nature communications

Article

https://doi.org/10.1038/s41467-025-58333-0

Molecular insights into the α6β4 nicotinic acetylcholine receptor function and ligand recognition

Received: 3 July 2024

Accepted: 17 March 2025

Published online: 02 April 2025

Check for updates

Jiawei Su[1,2,3,7], Zhuoya Yu[1,2,3,7], Zhengji Yin[4,5,7], Zixuan Zhang[4,5], Jun Zhao[6], Yufei Meng[1,2,3], Renjie Li[1,2,3], Yiwei Gao[1,2,3], Hongwei Zhang[1], Rilei Yu[4,5,7] ✉ & Yan Zhao[1,2,7] ✉

The α6β4 nicotinic acetylcholine receptor (nAChR) is found in the sensory neurons of dorsal root ganglia. It is a promising therapeutic target for pain. However, the difficultly of heterologous functional expression of α6β4 receptor has hindered the discovery of drugs that target it. Here, we functionally express the human α6β4 receptor and determine the cryo-EM structures of α6β4 receptor in complex with its agonists, nicotine and the preclinical drug tebanicline. These structures were captured in non-conducting desensitized states. We elucidate that the stoichiometry of α- and β- subunits in the α6β4 receptor is 2α6:3β4. Furthermore, we identify the binding pockets for nicotine and tebanicline, demonstrating the essential residues contributing to ligand affinity and providing detailed molecular insights into why these agonists have different binding affinities despite both occupying the orthosteric site of the α6β4 receptor. These structures offer significant molecular insight into the function and ligand recognition of α6β4 receptor.

Nicotinic acetylcholine receptors (nAChRs) were the first biochemically isolated neurotransmitter ion channels, exhibiting permeability to cations such as Ca^{2+}, Na^{+} and K^{+}[1–3]. They are ligand-gated ion channels present in the central and peripheral nervous systems and belong to the Cys-loop receptor superfamily[4]. Neuronal nAChRs form functional pentamers derived from nine α (α2-α10) and three β (β2-β4) subunits, resulting in a variety of subtypes in mammalian nervous system[5]. One of the predominant subtypes of nAChRs are α6-containing heteropentamers, which are predominantly distributed in the ventral tegmental area (VTA), nucleus accumbens (NAc) and spinal cord[6,7]. In mice, reducing the expression level of α6 decreased the dopamine release and attenuated the stimulatory effects of some analgesic drugs[8–11]. Therefore, the α6-containing nAChRs have been served as many pharmacological targets such as nicotine addiction, Parkinson's disease, and antiallodynia[12,13].

One of the well-studied pharmacologically significant α6-containing nAChRs is the α6β4 subtype. It expresses in the sensory neurons of dorsal root ganglia (DRG), which play important roles in pain perception and transmission[14,15]. In recent years, increasing studies have reported that the α6β4 receptor is involved in pain modulation. For example, in mice, the agonists of α6β4, such as nicotine and tebanicline, act as effective analgesics to alleviate pain[10,16].

[1]National Laboratory of Biomacromolecules, CAS Center for Excellence in Biomacromolecules, Institute of Biophysics, Chinese Academy of Sciences, Beijing 100101, China. [2]State Key Laboratory of Brain and Cognitive Science, Institute of Biophysics, Chinese Academy of Sciences, 15 Datun Road, Beijing 100101, China. [3]College of Life Sciences, University of Chinese Academy of Sciences, Beijing 100049, China. [4]Key Laboratory of Marine Drugs, Chinese Ministry of Education, School of Medicine and Pharmacy, Ocean University of China, Qingdao 266003, China. [5]Laboratory for Marine Drugs and Bioproducts, Qingdao Marine Science and Technology Center, Qingdao 266237, China. [6]Peking University Institute of Advanced Agricultural Sciences, Shandong Laboratory of Advanced Agricultural Sciences at Weifang, Weifang, Shandong 261000, China. [7]These authors contributed equally: Jiawei Su, Zhuoya Yu, Zhengji Yin, Rilei Yu, Yan Zhao. ✉e-mail: ryu@ouc.edu.cn; zhaoy@ibp.ac.cn

However, the efficacy of these analgesics decreases when the expression of α6β4 is reduced[10,15]. Therefore, the α6β4 receptor has been considered an appealing therapeutic target for pain. Despite its potential as a pain target, drug discovery and basic science efforts have been hindered for a long time because it is not expressed functionally in any recombinant system[8]. Recently, the discovery of chaperone proteins (BARP, IRE1α and SULT2B1) enabled functional heterologous expression of the α6β4 receptor, facilitating its systematic study[10].

Here, we determined the structures of α6β4 bound with its agonists, nicotine and tebanicline. These structures are stabilized in non-conducting desensitized states, which allows us to understand the molecular insights into subunit assembly, ligand recognition, and ion permeation pathway in α6β4 receptor.

Results and discussion

Structural determination of α6β4 nicotinic acetylcholine receptor

To gain molecular insights into the α6β4 receptor, we co-expressed wild type (WT) human α6 and β4 subunits, along with their protein chaperones (IRE1, SUL2B1 and BARP) in HEK293 cells[10]. However, the WT α6β4 receptor exhibited protein heterogeneity and poor expression in HEK293 cells, presenting challenges for structural studies (Supplementary Fig. 1a). To optimize the biochemical properties and structural stability of the α6β4 receptor, we substituted a segment of the intracellular M3-M4 loop in the full-length wild-type (WT) α6 (residues L345-L385) and β4 (residues F340-P378) genes with superfolder GFP and a thermostable protein (bRIL). Additionally, we introduced several mutations within the MA helix situated at intracellular domain (ICD) of the WT α6 and β4 genes (Supplementary Fig. 1b, c). We named this construct as $α6β4^{EM}$. We obtained robust current responses from the $α6β4^{EM}$ construct using two-electrode voltage clamp experiments in *Xenopus* oocytes, suggesting that this construct is functional. Further analysis revealed that $α6β4^{EM}$ exhibited similar affinities for nicotine (EC_{50} = 33 μM) compared with the WT full-length α6β4 (EC_{50} = 21.6 μM) (Fig. 1a, b). Additionally, the $α6β4^{EM}$ construct expressed well and the purified $α6β4^{EM}$ protein sample exhibited a symmetric profile on size-exclusion chromatography and SDS-PAGE shows two prominent bands (α6 and β4 subunits) (Supplementary Fig.1a, d). Thus, the $α6β4^{EM}$ construct was subjected to single particle cryo-electron microscopy (cryo-EM) analysis. We incubated the

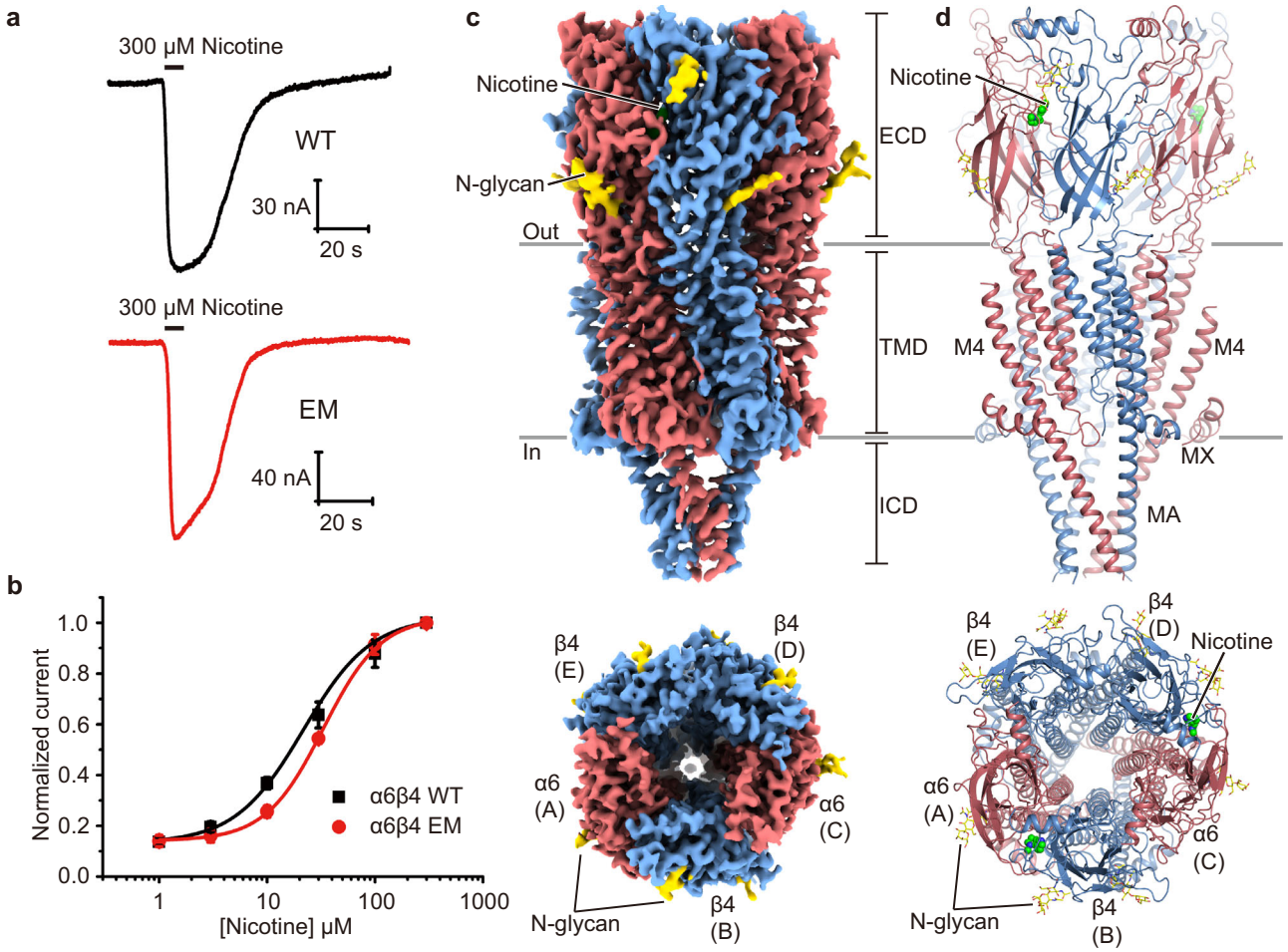

Fig. 1 | Architecture of human α6β4 receptor. a Representative traces of 300 μM nicotine-evoked current amplitude mediated by $α6β4^{WT}$ (Top) and $α6β4^{EM}$ (Bottom) nAChRs in *Xenopus* oocyte. The time course of nicotine application is indicated by the bars above the current traces. **b** Whole-cell concentration-response relationship of relative nicotine-evoked current amplitude comparing $α6β4^{WT}$ and $α6β4^{EM}$ in two-electrode voltage clamp experiment. The black and red curves represent $α6β4^{WT}$ and $α6β4^{EM}$, respectively .$α6β4^{WT}$ EC_{50} = 21.6 ± 2.7 μM (mean ± S.E.; 95% CI: 10.2–33.0 μM; *n* = 6, data from several experiments were pooled and each data point represents the average of 6 cells ±S.E.). $α6β4^{EM}$ EC_{50} = 33.0 ± 0.8 μM (mean ± S.E.; 95% CI: 29.6–36.5 μM; *n* = 6, data from several experiments were pooled and each data point represents the average of 6 cells ±S.E.). **c** The Cryo-EM maps of representative α6β4 receptor bound with nicotine, viewed parallel (Top) and perpendicular (Bottom) to the membrane. The density of the α6 and β4 subunits are colored in burgundy and blue, respectively. The glycosylation and nicotine are colored yellow and green, respectively. ECD Extracellular domain, TMD Transmembrane domain, ICD Intracellular domain. **d** Overall structure of representative structure bound with nicotine, viewed in parallel (Top) and perpendicular (Bottom) to the membrane. The density of α6 and β4 subunits are colored in burgundy and blue, respectively. The glycosylation and nicotine are colored yellow and green, respectively.

purified sample with different ligands, and determined the structures of α6β4 in complex with nicotine ($α6β4^{nico}$) and tebanicline ($α6β4^{teb}$) at resolutions of 3.3 Å and 3.2 Å, respectively (Supplementary Figs. 2, 3; Supplementary Table 1).

The cryo-EM maps of the α6β4 receptors were rich in structural features, including densities for side chains, N-glycans, disulfide bonds, waters, as well as associated ligands. These features enabled us to unambiguously build the α6β4 complex. The overall structure of α6β4 receptor has a cylinder-like shape (Fig. 1c, d). The α6 and β4 subunits are distinguishable according to the N-glycosylation in β4 subunit. $N138^{β4}$, located in the extracellular domain (ECD), is specific to the β4 subunits. Furthermore, the non-conserved residues of α6 and β4 subunits, such as $T133^{α6}$-$K137^{β4}$ and $V254^{α6}$-$F255^{β4}$, exhibit markedly different side chains, which match well with their EM densities (Supplementary Fig.4a, b). Therefore, we accurately determined that the α6β4 receptor consists of two α6 subunits and three β4 subunits, with a subunit arrangement of α6-β4-α6-β4-β4 around the pentameric ring (Fig. 1c, d). Each subunit comprises an extracellular domain (ECD), transmembrane domain (TMD) and intracellular domain (ICD). The ECD includes an N-terminal α-helix and ten β-strands that form a β-sandwich connecting to the M1 helix (Supplementary Fig.5a, b). A conserved disulfide bond located at the bottom of ECD linked β6 and β7 strands, with the linker between β6 and β7 strands representing the signature cys-loop found across all members of the superfamily (Supplementary Fig. 5a-c). The TMD includes four transmembrane (TM) helixes, M1-M4, and M2 lining the ion conducting pore. The ICD contains MA helix, an amphipathic MX helix and a disordered loop between MA and MX helices (Supplementary Fig. 5a, b). Superimposition of the α6 and β4 subunits of α6β4 revealed minor conformational differences (Supplementary Fig. 5d). Notably, a disulfide bond is present in the loop C of α6 but absent in β4, which is a feature that distinguishes nicotinic receptor α subunits from β subunits (Supplementary Fig. 5a-c).

Assembly of α6β4 nicotinic acetylcholine receptor

Some nAChRs assemble into two stoichiometries of α- and β- subunits (2α:3β and 3α:2β), Both assemblies are functional and have different biophysical properties, such as ligand binding affinity, ion permeability, and channel conductance[17,18]. The α6β4 receptor contains five interfaces, including two α6-β4 interfaces, two β4-α6 interfaces and one β4-β4 interface (Fig. 1c, d). Within the α6-β4 interface, residues of D152, E155 (in loop B of α6 subunit) and R83 (in β4 subunit) form two electrostatic interactions, that are conserved at both the β4-α6 and β4-β4 interfaces (Supplementary Fig. 6a-c). D152 and R83 are conserved in both α4β2 and α3β4 receptors (Supplementary Fig. 6d), and similar electrostatic interactions between these amino acids are also present in the structures of α4β2 and α3β4[19,20]. However, E155 is not conserved among nAChRs, and the associated electrostatic interactions (E-Rs) are specifically present in α6β4 among previously reported nAChR structures[19–22]. To investigate the functional role in α6β4 receptor, we evaluated the peak currents for WT α6β4 receptor and some mutants, including E155A, E155W, and E155F. Two-electrode voltage clamp experiments revealed that these three mutations significantly reduced current amplitudes (Supplementary Fig. 6e). Therefore, we hypothesized that this triad of electrostatic interactions is pivotal in the subunit assembly of α6β4. Additionally, a cation-π interaction between $F18^{α6}$ and $R88^{β4}$, several hydrogen bonds, such as $S127^{α6}$- $Q43^{β4}$, $W149^{α6}$-$L123^{β4}$, $N181^{α6}$- $D172^{β4}$ and $S267^{α6}$- $K210^{β4}$, as well as hydrophobic interactions, are present at the α6-β4 interface. Notably, a fenestration specifically formed at the β4-β4 interface comprises numerous polar residues and is larger (more than 6 Å) than hydrated ions (Supplementary Fig. 6f). Therefore, we predict that hydrated ions can permeate through this fenestration. A similar fenestration is also present at the β2-β2 interface[19].

The coupling region, which encompasss the β1-β2 loop, β6-β7 loop (Cys-loop), β8-β9 loop, pre-M1 linker, and M2-M3 loop, is important for coupling agonist binding to channel opening[23,24] (Supplementary Fig. 5a, b and 7a). Within this region, it is noteworthy that the residue V46 in α6 ($V46^{α6}$) is not conserved among nAChRs and the equivalent residue of V46 in α7 is K45 (Supplementary Fig. 7b). To investigate the functional role of V46 in α6β4 receptor, we generated a $V46K^{α6}$ mutant. Two-electrode voltage clamp experiments revealed that the rate of desensitization of V46K mutation was significantly faster than that of WT receptor (Supplementary Fig. 7d). Structural comparisons between the desensitization states of α6β4 and α7 receptors provided additional insights. In the α7 receptor, the K45-equivalent residue of V46 in α6, forms an inter-subunit electrostatic interaction with E172 in the desensitized state[25] (Supplementary Fig. 7c), potentially stabilizing the receptor in this state more rapidly. In contrast, this interaction is absent in α6β4 receptor structure, which may explain its slower desensitization rate compared to α7. Additionally, two intra-subunit electrostatic interactions occur in α6 between E45, D138 and R208 (Supplementary Fig. 7e), with this triad of electrostatic interactions serving as a conserved coupling element among most nAChRs[22,25–28].

In our cryo-EM data analysis, only one subunit stoichiometry of α6β4 receptor, 2α6:3β4, was present. To explain why other theoretically possible subunit stoichiometries were not present, we aligned the subunits pairwise based on the α6β4 receptor structure obtained in our experiment, which allowed us to generate theoretical pentameric models, including the 5β4 and 1α6:4β4 assemblies. These models were then optimized using energy minimization (Supplementary Fig. 8a). We observed a gap between subunits in both the 5β4 and 1α6:4β4 models. In the 1α6:4β4 model, distances between C132, K276, T291 (in chain E) and E172, I215, L230 (in chain A) ranged from 11.1 Å, 10.3 Å, 10.3 Å to 12.8 Å, 12.7 Å, 12.6 Å, respectively. The large decrease in surface area buried compared to the experimental model was also observed (1145.8 $Å^2$ versus 2188.2 $Å^2$) (Supplementary Fig. 8b, c). Similarly, in the 5β4 model, distances between T147, Y277, T291 (in chain D) and F174, I119, L231 (in chain E) ranged from 18.3 Å, 18.4 Å, 10.6 Å to 19.6 Å, 19.6 Å, 12.4 Å, respectively. Furthermore, a large decrease in surface area buried compared with the experimental model was observed (1023.3 $Å^2$ versus 1892.2 $Å^2$) (Supplementary Fig. 8b, d). Therefore, we hypothesized that the 2α6:3β4 form was more stable than the 5β4 and 1α6:4β4 forms under our experimental conditions.

Binding and recognition of nicotine

In the extracellular domain of the $α6β4^{nico}$ structure, loop C in α6 is closed while in β4 is open (Fig. 2a) and nicotine is situated inside the closed loop C. The nicotine binding pocket is located at the α6-β4 interface and is formed by residues from six loops: loops A-C form the principal side and loops D-F form the complementary side (Fig. 2b). Nicotine is surrounded by a cage of five highly conserved aromatic residues, including Y93 on loop A, W149 on loop B, Y190 and Y197 on loop C of the α subunit, and W59 on the β complementary side (Fig. 2c). The basic nitrogen of nicotine in the pyrrolidine ring formed a hydrogen bond with the backbone carbonyl of W149, along with a cation-π interaction with the aromatic side chain of this residue (Fig. 2c). Furthermore, the distance between the hydrogen on the nitrogen of pyrrolidine ring and the carbonyl of W149 remains stable during molecular dynamics simulations, which is consistent with our structural observations in the nicotine binding pocket (Fig. 2d; Supplementary Fig. 9a, Supplementary Table 2). Previous research also demonstrated that the W149 is essential for ligand binding to the α6β4 receptor[29]. Additionally, some hydrophobic interactions were present between nicotine and the conserved aromatic residues, including W59, Y93, W149, Y190, and Y197.

https://doi.org/10.1038/s41467-025-58333-0

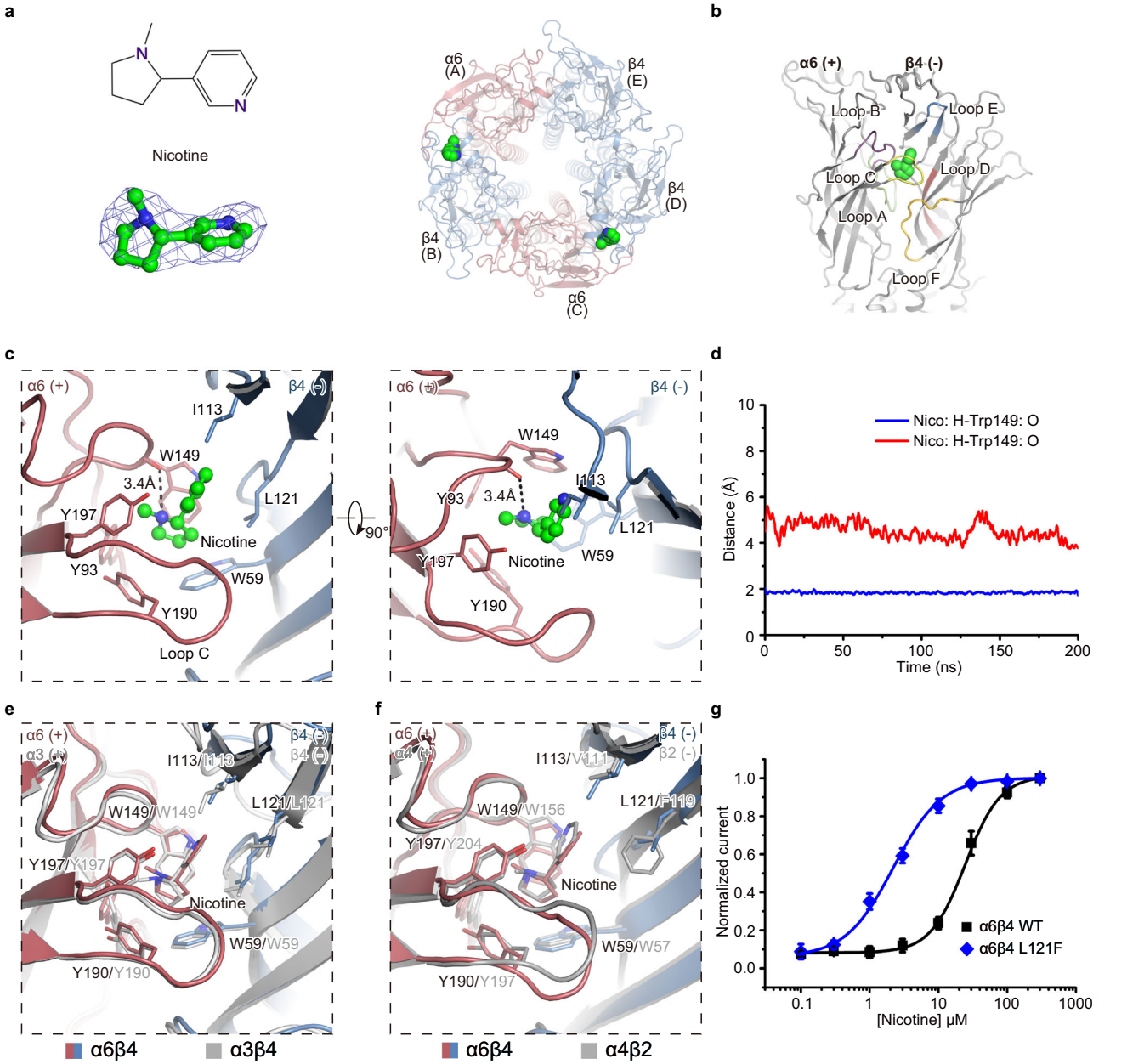

Fig. 2 | Nicotine binding site. a Left, the chemical structure of nicotine and the nicotine (cyan sticks) overlaid with its corresponding EM density (Blue mesh). Right, the top view of α6β4 structure bound with nicotine. **b** Loop A-F forming the nicotine binding pocket. Loop A-F are shown as different colors. Nicotine is showed as green spheres. **c** Interaction of nicotine in binding pocket. The key residues for interaction are showed as sticks. The nicotine is showed as sticks and spheres. The potential hydrogen bonds are represented as dashed lines. **d** Binding stability of nicotine in molecular dynamics simulations. Binding of nicotine measured by the distances from the hydrogen on the nitrogen of pyrrolidine ring to the carbonyl of W149 (blue line), and from the nitrogen of pyrrolidine ring to the carbonyl of L121 (red line). **e** Comparison of nicotine binding pocket in α6β4 and α3β4 receptors. The α3β4 receptor is colored as gray. The key residues for interaction in α6β4 and α3β4 receptors are represented by sticks and labeled. **f** Comparison of nicotine binding pocket in α6β4 and α4β2 receptors. The α4β2 receptor is colored as gray. The key residues for interaction in α6β4 and α4β2 receptors are represented by sticks and labeled. **g** Whole-cell concentration-response relationship of relative nicotine-evoked current amplitude comparing $α6β4^{WT}$ and $α6β4^{L121F}$ in two-electrode voltage clamp experiment. The black and blue curves represent $α6β4^{WT}$ and $α6β4^{L121F}$, respectively. $α6β4^{WT}$ EC_{50} = 24.6 ± 1.5 μM (mean ± S.E.; 95% CI: 20.3–28.8 μM; n = 4, data from several experiments were pooled and each data point represents the average of 4 cells ±S.E.). $α6β4^{L121F}$ EC_{50} = 2.2 ± 0.4 μM (mean ± S.E.; 95% CI: 1.1–3.3 μM; n = 4, data from several experiments were pooled and each data point represents the average of 4 cells ± S.E.).

To investigate why the ligands were not present at the β4-α6 or β4-β4 interface, we compared the conserved aromatic residues involved in ligand binding at the α6-β4 interface with those at β4-α6 or β4-β4 interface. We noticed a reorganization of these conserved aromatic residues in the β4-α6 and β4-β4 interfaces. Specifically, Y198 in loop C oriented toward the membrane, while Y97 in loop A rotates away from the membrane. Additionally, W153 in loop B rotates completely out of the binding pocket. Notably, residue G147 in α6 was replaced by R151 in β4, and the side chain of R151 directly inserts into the base of the ligand binding pocket (Supplementary Fig. 9c, d). Therefore, we speculate that the positively charged guanidinium group of R151 disrupts the hydrophobic cavity, leading to reorganization of the aromatic side chains. In the α4β2 structure, a previous study mentioned that R149 (equivalent to R151 in α6β4) forms cation-π

https://doi.org/10.1038/s41467-025-58333-0

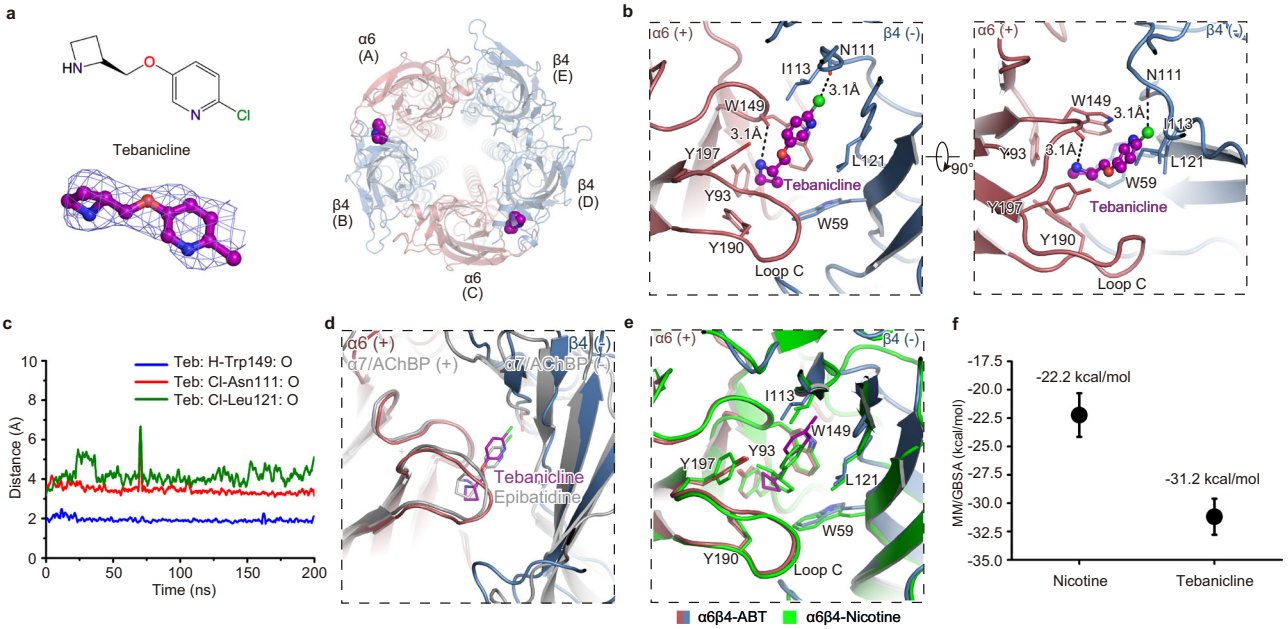

Fig. 3 | Tebanicline binding site. a Left, the chemical structure of tebanicline and the tebanicline (purple sticks) overlaid with its corresponding EM density (Blue mesh). Right, the top view of α6β4 structure bound with tebanicline. The α6 and β4 subunits are colored in burgundy and blue, respectively. The tebanicline is showed as spheres. **b** Interaction of tebanicline in binding pocket. The key residues for interaction are showed as sticks. The tebanicline is showed as sticks and spheres. The potential hydrogen bonds are represented as dashed lines. **c** Binding stability of tebanicline in molecular dynamics simulations. Binding of tebanicline measured by the distances from the hydrogen on the nitrogen of azetidine to the carbonyl of W149 (blue line), from the nitrogen of chloropyridine ring to the carbonyl of L121 (green line), and from the chlorine atom to the carbonyl oxygen of N111 (red line). **d** The ligand binding pockets of α6β4 and α7/AChBP chimera structures (corresponding to Fig. 2c). The structures of α6β4 and α7/AChBP are shown as cartoon. The of α6 and β4 subunits are colored in burgundy and blue, respectively, while the structure of α7/AChBP is colored in gray. Tebanicline and epibatidine molecules are shown as purple and gray sticks, respectively. **e** Comparison of nicotine and tebanicline binding pocket. The nicotine binding pocket is colored as green. The key residues for interaction are represented by sticks and labeled. Tebanicline and nicotine are colored as purple and green, respectively. **f** Predicted binding affinities of nicotine and tebanicline from MM/GBSA simulations. MM/GBSA energies were compute from the 50 frames extracted from the last 50 ns MD simulations. Nicotine: −22.2 ± 1.925 kcal/mol (mean ± S.E.); Tebanicline: −31.2 ± 1.5894 kcal/mol (mean ± S.E.).

interactions with surrounding aromatic residues (Supplementary Fig. 9e), functioning as a pseudo-agonist[26]. However, in the non-ligand binding site of α6β4 structure, the interactions between R151 and these aromatic residues were absent (Supplementary Fig. 9f, g). Similar phenomena were also observed in the α3β4 structure[27](Supplementary Fig. 9h). Therefore, we hypothesize that R151 and its equivalent residues play a non-equivalent role in receptors with distinct subunit compositions.

Nicotine, the agonist, activates various nAChRs, such as α6β4, α4β2 and α3β4. However, its affinity for α6β4 is similar to that for α3β4, while is 20–100 times lower than for α4β2. Therefore, we compared the nicotine-bound structure of α6β4 with those of α4β2 and α3β4, respectively[26,27]. Superposing the binding pockets of α6β4 and α3β4 revealed the conservation of all residues, and their similar orientations, resulting in similar binding affinities for nicotine (Fig. 2e). However, several differences were observed between the nicotine binding pockets of α6β4 and α4β2. First, loop C in α6 is situated farther away from the agonist binding pocket compared to loop C in α4. Second, residues I113 and L121 in β4 are equivalent to V111 and F119 in β2. We speculated that the L121F substitution engage in a π-π interaction between the aromatic side chain of phenylalanine and the pyridine moiety of nicotine, resulting in the higher affinity of α4β2 for nicotine than that of α6β4 (Fig. 2f). A similar difference was also observed between α4β2 and α3β4 structures[27]. Two-electrode voltage clamp experiments indicated that the L121F mutation in β4 increased the binding affinity of α6β4 for nicotine by approximately 10-fold (Fig. 2g), supporting our prediction that the interaction between the aromatic side chain of phenylalanine and nicotine improved nicotine affinity.

Binding and recognition of tebanicline

Tebanicline (ABT-594), an agonist of α6β4, exhibits potent analgesic activity against neuropathic pain[10,30–32]. In the structure of $\alpha6\beta4^{teb}$, tebanicline is present in the orthosteric binding site located in the ECD at the α6-β4 interface (Fig. 3a). Its azetidine moiety points toward the principal subunit, interacting with the conserved aromatic residues, while the chloropyridine ring faces the complementary subunit. Specifically, the nitrogen of azetidine ring formed a hydrogen bond with the backbone carbonyl of W149 and engaged in a cation-π interaction with the aromatic side chain of this residue. The chlorine atom forms a halogen bond with the carbonyl oxygen of N111 (Fig. 3b). During our molecular dynamics simulations, the distances between the hydrogen on the nitrogen of azetidine and the carbonyl of W149, as well as the chlorine atom and the carbonyl oxygen of N111, remained stable, supporting our structural observations (Fig. 3c; Supplementary Fig. 9a, Supplementary Table 2). Similar interactions between the chlorine atom and the carbonyl group on the complementary face of the orthosteric binding site was observed in the structures of a soluble α7-AChBP nicotinic receptors[33] (Fig. 3d). Additionally, some hydrophobic interactions are present between tebanicline with the residues W59, Y93, W149, Y190, and Y197. To elucidate the activation mechanism of tebanicline, which exhibits approximately 50 times higher affinity for α6β4 than nicotine, we compared the structures of the $\alpha6\beta4^{teb}$ and $\alpha6\beta4^{nico}$. We observed a similar orientation of residues and ligand–receptor interactions in these two binding pockets. Both nicotine and tebanicline formed hydrogen bonds and cation–π interactions with the residue W149. However, a halogen bond between the chlorine atom and the carbonyl oxygen of N111 is present in the tebanicline binding pocket but absent in the nicotine binding pocket (Figs. 2c and 3b, e). Furthermore,

https://doi.org/10.1038/s41467-025-58333-0

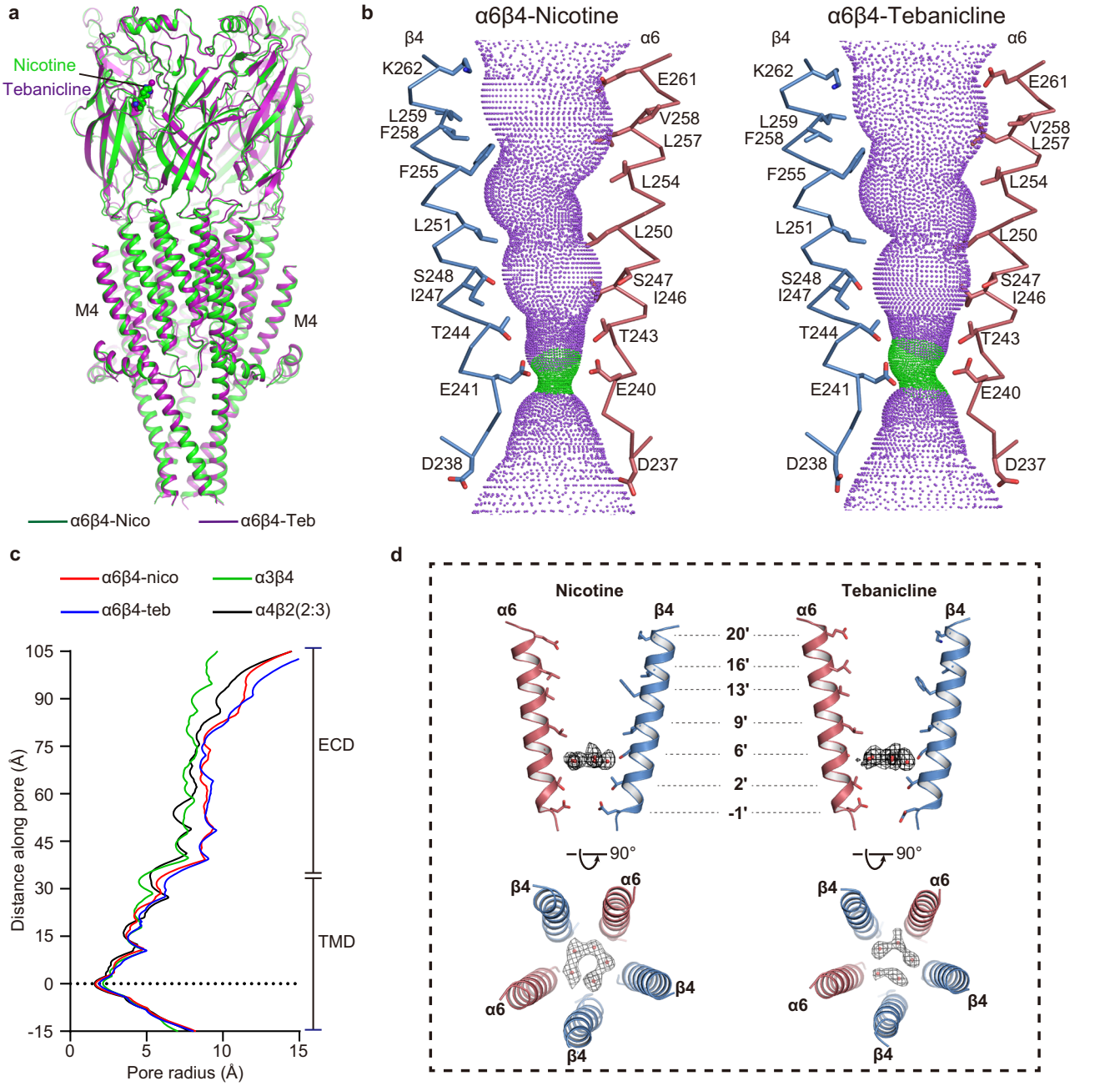

Fig. 4 | The permeation pathway of α6β4 receptors. a Comparison of the structures of $α6β4^{nico}$ and $α6β4^{teb}$. The $α6β4^{nico}$ and $α6β4^{teb}$ are colored green and purple, respectively. **b** M2 α-helices from opposing α6 (burgundy) and β4 (blue) subunits with the sidechain shown for pore-lining residues. Purple spheres indicate pore diameter over 5.6 Å; green spheres are 2.8–5.6 Å. **c** Pore radius for the $α6β4^{nico}$, $α6β4^{teb}$, α3β4 (PDB accession: 6pv7) and α4β2 (PDB accession: 6cnj). The zero value along the y-axis of the plot is aligned with the α-carbon of the −1 position. **d** Position of water pentagons in the pore and corresponding density, viewed in parallel (Top) and perpendicular (Bottom) to the membrane. Opposing α6 and β4 subunits with the sidechain shown for pore-lining residues are colored burgundy and blue, respectively. The water is shown as spheres and colored in red.

we calculated the binding free energy (ΔG-bind) using MM/GBSA, and the ΔG-$bind^{teb}$ (−31.2 kcal/mol) was lower than ΔG-$bind^{nico}$ (−22.2 kcal/mol), indicating that the ligand binding pocket is more stable in $α6β4^{teb}$ than in $α6β4^{nico}$ (Fig. 3f). These structural comparisons and molecular dynamics simulations between $α6β4^{teb}$ and $α6β4^{nico}$ provide initial insights into the different ligand sensitivities of nicotine and tebanicline.

Permeation pathway of the α6β4 nicotinic acetylcholine receptor

Binding of agonists to their nicotinic acetylcholine receptor induces conformational transitions from the resting state to the activated state, enabling ion permeation. In the sustained presence of agonists, most nAChRs are desensitized, adopting an agonist-bound, closed pore conformation. The structures of $α6β4^{nico}$ and $α6β4^{teb}$ are nearly identical, with a r.m.s. deviation (r.m.s.d.) of 0.75 Å for 1884 Cα atoms (Fig. 4a). Their ion permeation pathway contains a wide extracellular vestibule, a funnel-shaped TMD pore narrowing the cytoplasm, and an intracellular domain. The TMD pore contains a hydrophobic gate near its midpoint of the pore and a desensitized gate near the cytosolic end of the channel. The hydrophobic gate comprises residues at the 9′ (Leu), 13′ (Val) and 16′ (Leu) positions, and the pore diameters at the 9′, 13′ and 16′ positions are more than 7 Å, which is sufficiently large to

allow the passage of hydrated cations (Fig. 4b and Supplementary Fig. 10a). The desensitized gates are formed by the side chains of polar glutamates at the −1′ position, with a pore diameter of approximately 3.5 Å (Fig. 4b and Supplementary Fig. 10a). Therefore, we propose that our structures represent a non-conducting, agonist-bound desensitized state. Comparisons with desensitized structures of other desensitized heteropentamer nAChRs, like α3β4 and α4β2 receptors, revealed the conservation of residues at 9′, 13′,16′ and −1′ positions (Supplementary Fig. 10b) and the congruent pore radius (Fig. 4c). After the ions pass through the TMD pore, hydrated ions proceed through the lateral ICD portals to the cytosol[20].

Within the pore, a pentagonal ring of water is present near the polar residues of Ser6′, which are crucial for channel conductance[34](Fig. 4d). Analogous water pentagons have been found in the structures of α3β4, muscle-type nicotinic receptors, and prokaryotic pentameric ligand-gated ion channels[20,35].

Discussion

In our study, we determined the structures of α6β4 in complex with the agonist nicotine and the preclinical drug tebanicline. The α6β4 receptor assembles with a stoichiometry of 2α6:3β4. We hypothesize that the conserved triad of electrostatic interactions, including $E155^{\alpha6}$-$R83^{\beta4}$ and $D152^{\alpha6}$-$R83^{\beta4}$, is pivotal in the subunit assembly of α6β4. Within the ligand binding pocket, in addition to the five highly conserved aromatic residues crucial for ligand–receptor interactions, the residue L121 in loop E is also essential for ligand binding, similar to its function in α4β2 structure[27]. Furthermore, we observed that tebanicline occupies the orthosteric sites in the structure of $\alpha6\beta4^{teb}$. The presence of a halogen bond between the chlorine of tebanicline and carbonyl oxygen of N111 in β4 subunit may explain the higher binding affinity of tebanicline for α6β4 than nicotine. Additionally, the desensitized α6β4 receptor features a funnel-shaped TMD pore, with the diameter of the resting gate being more than 7.0 Å and the desensitized gate being approximately 3.5 Å. Taken together, our study elucidates the molecular mechanisms of α6β4 receptor function and ligand recognition mechanism, providing a platform for structure-based drug design.

Methods

Expression and protein purification of the human α6β4 nicotinic receptor

Genes encoding the human α6β4 nicotinic receptor subunits, α6 (UniProt Accession: Q15825) and β4 (P30926), were synthesized. The residues Ala345–Pro385 of the α6 subunit were replaced by a superfolder GFP with HRV-3C sites at both its N-terminal and C-terminal ends. The residues Pro340–Ser398 of the β4 subunit were replaced by a thermostable protein (bRIL) with similar HRV-3C sites and C-terminal Twin-Strep tags. Several mutations have also been introduced into the ICDs of the α6 and β4 subunits. These modified genes were then subcloned into a modified pEG BacMam vector. Additionally, genes encoding accessory proteins essential for α6β4 receptor, including IRE1 (UniProt Accession: Q75460), SULT2B1 (UniProt Accession: O00204) and BARP (UniProt Accession: Q8N350) were synthesized and subcloned into the modified pEG BacMam vector. Protein expression utilized the Bac-to-Bac baculovirus expression system in Sf9 cells, cultured in IB905 Medium (YSK BIOSCIENCES, Zhejiang, China), with α6β4 receptor and accessory proteins co-infected into HEK293F cells (2.5×10^6 cells/ml, Gibco, USA) using multiple P2 baculovirus vectors (1%, v/v). The cells were cultured in 293F Hi-exp Medium (AC601501, Shanghai OPM Biosciences Co., Ltd) at 37 °C in a 5% CO_2 shaking incubator and 10 mM sodium butyrate was added to the culture 12h after infection. Cells were harvested 48h post-infection, flash-frozen using liquid nitrogen, and stored at −80 °C.

HEK293F cells expressing the human α6β4 nicotinic receptor were resuspended in a purification buffer (20 mM HEPES pH 7.5 (High Purity Grade, JS0164, JSENB), 150 mM NaCl, 0.8 μM aprotinin (MedChemExpress), 2 μg/mL leupeptin (MedChemExpress), and 2 μM pepstatin A (MedChemExpress)). Cell membranes were extracted using a Dounce homogenizer and collected by ultracentrifugation at 50,000 g for 1 h. The resulting membranes were resuspended and solubilized by the addition of 1% (w/v) n-dodecyl-β-D-maltoside (DDM) (Anatrace, USA) and 0.15% (w/v) cholesteryl hemisuccinate (CHS) (Anatrace, USA), on a rotating mixer at 4 °C for 2 h. ATP and MgCl2 were added to remove associated heat shock proteins. The cell debris was removed through a second ultracentrifugation at 50,000 g for 1 h. The supernatant was filtered and loaded into pre-equilibrated Streptactin Beads (Smart-Lifesciences, China), and the column was washed with 10 column volumes of the purification buffer supplemented with 0.03% glycodiosgenin (GDN, Anatrace, USA). The protein was eluted with an elution buffer (20 mM HEPES pH 7.5, 150 mM NaCl, 0.03% (w/v) GDN, and 5 mM desthiobiotin (1169249, Leyan)) and incubated together with 0.5 mg His-tagged PPase to digest sfGFP and bRIL. The digested protein sample was concentrated to 1 mL using a 100-kDa MWCO Amicon (Millipore, USA). The concentrated protein sample was further purified by gel-filtration (Superose-6 Increase 10/300 GL, GE Healthcare, USA) with a running buffer (20 mM HEPES pH 7.5, 150 mM NaCl, and 0.007% (w/v) GDN). Peak fractions were pooled and concentrated to 10 mg/mL using a 100 kDa MWCO Amicon filter (Amicon Ultracel-100, Merck Millipore, Ireland) for cryo-EM sample preparation. The final protein samples used in the cryo-EM study were analyzed by SDS-PAGE, with molecular weight protein markers (New Cell & Molecular Biotech, P9008) used for reference.

Cryo-EM sample preparation and data collection

A final concentration of 1 mM nicotine or tebanicline was added to the cryo-EM samples for $\alpha6\beta4^{nico}$ and $\alpha6\beta4^{teb}$, respectively, and the samples were incubated 30 min on ice before being applied to the grids. Grids (Quantifoil Cu R1.2/1.3 300 mesh) were glow-discharged in the presence of H_2 and O_2 for 60 s. The glow-discharged grids were applied with a 2.5 μl droplet of prepared sample and then blotted for 4–6 s at 4 °C under condition of 100% humidity and then vitrified in liquid ethane using a Vitrobot Mark IV (Thermo Fisher Scientific, USA).

Cryo-EM data were collected using an EPU (Thermo Fisher Scientific) on a 300-kV Titan Krios G4 (Thermo Fisher Scientific) equipped with a K3 direct electron detector (Gatan, USA) and a GIF-Quantum LS energy Filter (Gatan, USA; slit width 20 eV). The movies were collected with a nominal magnification of 105000× in super-resolution mode, yielding a pixel size of 0.85 Å on images. The dose rate was set to ~20 e − /(pixel*s) with a defocus value ranging from −1.0 to −2.0 μm. Each movie stack was dose-fractioned into 32 frames and recorded with a total dose of ~60 e − /$Å^2$. The dose rate was set to 15 e−/pixel/s. The statistics of cryo-EM data are summarized in Supplementary Table 1.

Cryo-EM data processing

For the nicotine-bound dataset, a total of 2835 movies were collected. Motion correction and CTF parameter estimation were performed using the Patch Motion Correction (MotionCor2 v1.4.7) and Patch CTF (Gctf v1.18) Estimation programs in CryoSPARC, respectively[36–38]. Subsequently, 2816 micrographs were selected for particle picking after removing those exhibiting ice and ethane contamination and filtering based on a detected CTF estimation resolution better than 6 Å. The particle picking was performed using Blob picker in CryoSPRAC (CryoSPRAC v3.3.2), resulting in 1,090,739 particles which underwent several consecutive rounds of 2D classification. The 2D classes showing distinguishable features were chosen in each round, and the particles from the final round were used for ab-initio reconstruction, resulting in an initial map. The initial map was regarded as a good reference map for the following guided multi-reference 3D classification. Several rounds of guided multi-reference 3D classification were performed on the 1,090,739 particles against the initial map and 5

biased reference maps to sort good particles, which resulted in 67,470 particles. Non-uniform refinement (NU-Refinement) was performed to align these particles and generate a 3D reconstruction at 3.5 Å. To improve the density of the map, the refined particles were subjected to another round of 3D classification without alignment and with a mask excluding the micelles. Then, the particles belonging to the best 3D class were subjected to the local refinement with the excluding the micelles and resulting a final map at 3.3 Å.

A similar strategy was applied in the data processing of tebanicline-bound dataset. Specifically, a total of 3,256,486 particles were picked from 3795 micrographs and the final map of $\alpha6\beta4^{teb}$ was reported at 3.2 Å resolution. The diagrams of the data processing are summarized in Supplementary Fig. 2 and Supplementary Fig. 3.

Model building

The cryo-EM density maps of α6β4 nicotinic receptor showed clear densities of most sidechains, wihch allowed us to build and refine the models. De novo initial model of $\alpha6\beta4^{nico}$ was initiated using the 3.3 Å map, and the initial model was subsequently inspected, manually adjusted, and rebuilt in COOT (v0.9.8.1). The structure of $\alpha6\beta4^{nico}$ was used as an initial template and fitted to the EM map of $\alpha6\beta4^{teb}$ using UCSF Chimera (v1.3)[39]. Initial model of $\alpha6\beta4^{teb}$ was subsequently inspected, manually adjusted, and rebuilt in COOT[40]. The ligand models were generated using Ligand Builder in COOT, and its restraint file was generated using eLBOW in the PHENIX package (PHENIX V1.18.2)[41]. The α6β4 nicotinic receptor models were then automatically refined against the cryo-EM maps using the integrated Real Space Refinement program within the PHENIX software package[41]. Model stereochemistry was also evaluated using the Comprehensive Validation (Cryo-EM) tool in PHENIX.

All the figures were prepared using Open-source PyMOL (v2.5.5, Schrödinger, USA) and UCSF Chimera[39].

Preparation of cDNA and cRNA constructs

Plasmid DNAs encoding human α6 (UniProt Accession: Q15825) and β4 (P30926) nAChR subunits were synthesized. For expression in oocytes, all cDNAs were subcloned into the pBluescript KSM vector. cRNAs were transcribed in vitro using the T3 Mmessage Machine Kit (Ambion) after linearization of the pBluescript KSM construct with the NotI enzyme.

Oocyte preparation and microinjection

Oocytes were harvested from *Xenopus laevis* female clawed frogs after anesthesia. Oocytes were transferred to 15 mL tubes and then treated with 2 mg/mL collagenase (Sigma type II, Sigma-Aldrich Inc, USA) in Ca^{2+}-free OR2 solution (82.5 mmol/L NaCl, 2.5 mmol/L KCl, 1 mmol/L $MgCl_2$, and 5 mmol/L HEPES, pH 7.4) for about 20 min at 20–25 °C with gentle rotation and washed three times with OR2 solution, keeping them in sterile ND96 solution (96 mmol/L NaCl, 2 mmol/L KCl, 1.8 mmol/L $CaCl_2$, 1 mmol/L $MgCl_2$, 5 mmol/L HEPES, 550 mg/L sodium pyruvate, and 90 mg/L theophylline, pH 7.4, adjusted with NaOH), supplemented with 5% fetal bovine serum, 0.1 mg/mL gentamicin (Gibco, Grand Island, NY, USA) and 100 U/mL penicillin–streptomycin (Gibco, Grand Island, NY, USA). The oocytes were injected with 23 nL of cRNA solution containing approximately 10–20 ng of total cRNAs, which were injected in a 10:10:1 combination of human α6 subunits, human β4 (or its mutants) subunits and β-anchoring and -regulatory protein (BARP), using a microinjector (Drummond Scientific, USA). Oocytes were kept at 16 °C in ND96 solution.

Two-electrode voltage clamp recordings of α6β4 nicotinic receptor channels in *Xenopus* oocyte

Electrophysiological recordings were carried out 4–7 days post cRNA microinjection. Two-electrode voltage clamp recordings were performed at room temperature using a HEKA-iTEV90 amplifier and PatchMaster software (HEKA Instruments, Germany) at a holding potential of −70 mV. Oocytes were impaled with two microelectrodes (0.5–1.0 MΩ) filled with 3 mol/L KCl in a 40 µL recording chamber. Oocytes were perfused with ND96 solution using a distributor valve (ALA Corp., NY, USA) at a rate of 2 mL/min.

Initially, oocytes were briefly washed with ND96 solution followed by three repeated applications of the agonist for human α6β4 nAChR. Agonist solutions (freshly prepared from frozen stock aliquots) were applied via the bath perfusion at 5 min intervals for a period sufficient to obtain a stable plateau response at lower concentrations or a sag after a peak at higher concentrations). The 5 min intervals were sufficient to ensure reproducible responses. A standard concentration of nicotine was applied to every oocyte to monitor agonist sensitivity throughout the experiment. Experimental studies were started when the standard concentration of nicotine produced reproducible responses. For nicotine and tebanicline dose–response curves, the Hill1 equation was used to fit. To characterize desensitization, currents were evoked by 1 mM ACh at 1 min intervals with ND96 washout, and the time constant was measured by fitting the current decays with two-phase exponential association equation using Origin 9.0 software (OriginLab Corporation, Northampton, MA). All values were normalized to those produced by ACh for each individual cell. All solutions were prepared in ND96 solution containing 0.1% bovine serum albumin. Peak current amplitudes were measured using Igor Pro software (Wave-metrics).

All electrophysiological recordings were performed at room temperature and all electrophysiological data were analyzed with Igor Pro (Wave-metrics), Origin 9 (OriginLab) and GraphPad Prism (GraphPad Software, La Jolla, CA, USA). All electrophysiological data were pooled ($n \geq 4$) and represent means ± standard errors of the means. The EC_{50} was determined from concentration–response curve fitted to a non-linear regression function and reported with error of the fit.

Molecular dynamics simulations

MD simulations of the α6β4 nAChR were performed using AMBER20[42] with a ff19SB force field[43] for proteins and GAFF force field[44] for ligands. The complexes were solvated in an OPC water box, and the electrical properties were neutralized using Cl^- and Na^+. Once we built the whole system in xLeap of AMBER20[42], minimization before the MD simulation was performed to remove the van der Waals contacts between the ligands and α6β4 nAChR. The first step was constrained optimization, which was the steepest descent method optimization of 2000 steps and the conjugate gradient method optimization of 3000 steps, and the solute binding force was 100 kcal/mol^{-1}/Å^{-2}. After completing the first round of energy optimization, the binding force was removed from the solute molecules, unconstrained optimization was performed, and the entire system was optimized using the same parameters as above. Next, the whole system was gradually heated from 50 K to 300 K at a constant volume and temperature ensemble for 100 ps with the solute restrained with a harmonic force of 5 kcal/mol^{-1}/Å^{-2}. The simulations were then switched to constant pressure and temperature ensemble by maintaining the harmonic restraints for 100 ps. Then, 200 ns simulations were conducted at a constant temperature of 300 K and with pressure at 1 atm. The SHAKE algorithm was used for all the hydrogen bonds involved, and a time step of 2 fs was used. After the MD simulation, the MD trajectories were analyzed using VMD (http://www.ks.uiuc.edu/), and root mean square deviation (RMSD) values were calculated. The simulation results presented are independent of initial configuration and have equilibrated in the simulations.

Molecular mechanics generalized Born surface area (MM/GBSA)[45] was applied to calculate the binding affinities of ligands against the α6β4 nAChR. The energies were averaged on the 50 frames extracted from the last 50 ns of the MD simulations. The parameters are were

previously reported[46]. Briefly, the internal dielectric and external dielectric constants were set to 2.0 and 80.0, respectively. A probe radius of 1.4 Å, a grid spacing of 0.5 Å and an ionic strength 0.1 mol/L were used for the calculations.

Reporting summary

Further information on research design is available in the Nature Portfolio Reporting Summary linked to this article.

Data availability

The three-dimensional cryo-EM density maps of the $\alpha6\beta4^{nico}$ and $\alpha6\beta4^{teb}$ complexes have been deposited in the Electron Microscopy Data Bank under the accession codes EMD-60401 and EMD-60400, respectively. The coordinates for the $\alpha6\beta4^{nico}$ and $\alpha6\beta4^{teb}$ complexes have been deposited in the Protein Data Bank under accession codes 8ZRP and 8ZRN, respectively. The PDB codes of α4β2, α3β4, and soluble α7-AChBP nicotinic receptors are 6cnj (https://www.rcsb.org/structure/6CNJ), 6pv7 (https://www.rcsb.org/structure/6PV7), and 3sq6 (https://www.rcsb.org/structure/3SQ6), respectively. Source data are provided with this paper.

References

1. Hucho, F. & Changeux, J. P. Molecular weight and quaternary structure of the cholinergic receptor protein extracted by detergents from Electrophorus electricus electric tissue. *FEBS Lett* **38**, 11–15 (1973).
2. Changeux, J. P. Discovery of the First Neurotransmitter Receptor: The Acetylcholine Nicotinic Receptor. *Biomolecules* **10**, https://doi.org/10.3390/biom10040547 (2020).
3. Changeux, J. P., Kasai, M. & Lee, C. Y. Use of a snake venom toxin to characterize the cholinergic receptor protein. *Proc Natl Acad Sci USA* **67**, 1241–1247 (1970).
4. Sine, S. M. & Engel, A. G. Recent advances in Cys-loop receptor structure and function. *Nature* **440**, 448–455 (2006).
5. Gotti, C., Zoli, M. & Clementi, F. Brain nicotinic acetylcholine receptors: native subtypes and their relevance. *Trends Pharmacol Sci* **27**, 482–491 (2006).
6. Le Novère, N., Zoli, M. & Changeux, J. P. Neuronal nicotinic receptor alpha 6 subunit mRNA is selectively concentrated in catecholaminergic nuclei of the rat brain. *Eur J Neurosci* **8**, 2428–2439 (1996).
7. Quik, M., Polonskaya, Y., Gillespie, A., G, K. L. & Langston, J. W. Differential alterations in nicotinic receptor alpha6 and beta3 subunit messenger RNAs in monkey substantia nigra after nigrostriatal degeneration. *Neuroscience* **100**, 63–72 (2000).
8. Letchworth, S. R. & Whiteaker, P. Progress and challenges in the study of alpha6-containing nicotinic acetylcholine receptors. *Biochem Pharmacol* **82**, 862–872 (2011).
9. Kulak, J. M., McIntosh, J. M., Yoshikami, D. & Olivera, B. M. Nicotine-evoked transmitter release from synaptosomes: functional association of specific presynaptic acetylcholine receptors and voltage-gated calcium channels. *J Neurochem* **77**, 1581–1589 (2001).
10. Knowland, D. et al. Functional alpha6beta4 acetylcholine receptor expression enables pharmacological testing of nicotinic agonists with analgesic properties. *J Clin Investig* **130**, 6158–6170 (2020).
11. Gu, S. et al. alpha6-Containing Nicotinic Acetylcholine Receptor Reconstitution Involves Mechanistically Distinct Accessory Components. *Cell Rep* **26**, 866–874.e863 (2019).
12. Drenan, R. M. et al. In vivo activation of midbrain dopamine neurons via sensitized, high-affinity alpha 6 nicotinic acetylcholine receptors. *Neuron* **60**, 123–136 (2008).
13. Quik, M., Perez, X. A. & Grady, S. R. Role of alpha6 nicotinic receptors in CNS dopaminergic function: relevance to addiction and neurological disorders. *Biochem Pharmacol* **82**, 873–882 (2011).
14. Hone, A. J., Meyer, E. L., McIntyre, M. & McIntosh, J. M. Nicotinic acetylcholine receptors in dorsal root ganglion neurons include the α6β4* subtype. *Faseb j* **26**, 917–926 (2012).
15. Wieskopf, J. S. et al. The nicotinic α6 subunit gene determines variability in chronic pain sensitivity via cross-inhibition of P2X2/3 receptors. *Sci Transl Med* **7**, 287ra272 (2015).
16. Rowbotham, M. C., Duan, R. W., Thomas, J., Nothaft, W. & Backonja, M. M. A randomized, double-blind, placebo-controlled trial evaluating the efficacy and safety of ABT-594 in patients with diabetic peripheral neuropathic pain. *Pain* **146**, 245–252 (2009).
17. Moroni, M., Zwart, R., Sher, E., Cassels, B. K. & Bermudez, I. alpha4beta2 nicotinic receptors with high and low acetylcholine sensitivity: pharmacology, stoichiometry, and sensitivity to long-term exposure to nicotine. *Mol Pharmacol* **70**, 755–768 (2006).
18. Lester, H. A. et al. Nicotine is a selective pharmacological chaperone of acetylcholine receptor number and stoichiometry. Implications for drug discovery. *AAPS J* **11**, 167–177 (2009).
19. Walsh, R. M. Jr. et al. Structural principles of distinct assemblies of the human alpha4beta2 nicotinic receptor. *Nature* **557**, 261–265 (2018).
20. Gharpure, A. et al. Agonist Selectivity and Ion Permeation in the alpha3beta4 Ganglionic Nicotinic Receptor. *Neuron* **104**, 501–511.e506 (2019).
21. Noviello, C. M. et al. Structure and gating mechanism of the alpha7 nicotinic acetylcholine receptor. *Cell* **184**, 2121–2134 e2113 (2021).
22. Rahman, M. M. et al. Structure of the Native Muscle-type Nicotinic Receptor and Inhibition by Snake Venom Toxins. *Neuron* **106**, 952–962.e955 (2020).
23. Bouzat, C. et al. Coupling of agonist binding to channel gating in an ACh-binding protein linked to an ion channel. *Nature* **430**, 896–900 (2004).
24. Lee, W. Y. & Sine, S. M. Principal pathway coupling agonist binding to channel gating in nicotinic receptors. *Nature* **438**, 243–247 (2005).
25. Noviello, C. M. et al. Structure and gating mechanism of the α7 nicotinic acetylcholine receptor. *Cell* **184**, 2121–2134.e2113 (2021).
26. Morales-Perez, C. L., Noviello, C. M. & Hibbs, R. E. X-ray structure of the human α4β2 nicotinic receptor. *Nature* **538**, 411–415 (2016).
27. Gharpure, A. et al. Agonist Selectivity and Ion Permeation in the α3β4 Ganglionic Nicotinic Receptor. *Neuron* **104**, 501–511.e506 (2019).
28. Nemecz, Á., Prevost, M. S., Menny, A. & Corringer, P. J. Emerging Molecular Mechanisms of Signal Transduction in Pentameric Ligand-Gated Ion Channels. *Neuron* **90**, 452–470 (2016).
29. Maldifassi, M. C., Rego Campello, H., Gallagher, T., Lester, H. A. & Dougherty, D. A. Human α6β4 Nicotinic Acetylcholine Receptor: Heterologous Expression and Agonist Behavior Provide Insights into the Immediate Binding Site. *Mol Pharmacol* **103**, 339–347 (2023).
30. Bannon, A. W. et al. ABT-594 [(R)-5-(2-azetidinylmethoxy)-2-chloropyridine]: a novel, orally effective antinociceptive agent acting via neuronal nicotinic acetylcholine receptors: II. In vivo characterization. *J Pharmacol Exp Ther* **285**, 787–794 (1998).
31. Decker, M. W. et al. Antinociceptive effects of the novel neuronal nicotinic acetylcholine receptor agonist, ABT-594, in mice. *Eur J Pharmacol* **346**, 23–33 (1998).
32. Donnelly-Roberts, D. L. et al. ABT-594 [(R)-5-(2-azetidinylmethoxy)-2-chloropyridine]: a novel, orally effective analgesic acting via neuronal nicotinic acetylcholine receptors: I. In vitro characterization. *J Pharmacol Exp Ther* **285**, 777–786 (1998).
33. Li, S. X. et al. Ligand-binding domain of an α7-nicotinic receptor chimera and its complex with agonist. *Nat Neurosci* **14**, 1253–1259 (2011).

34. Imoto, K. et al. A ring of uncharged polar amino acids as a component of channel constriction in the nicotinic acetylcholine receptor. *FEBS Lett* **289**, 193–200 (1991).
35. Sauguet, L. et al. Structural basis for ion permeation mechanism in pentameric ligand-gated ion channels. *EMBO J* **32**, 728–741 (2013).
36. Zheng, S. Q. et al. MotionCor2: anisotropic correction of beam-induced motion for improved cryo-electron microscopy. *Nat Methods* **14**, 331–332 (2017).
37. Zhang, K. Gctf: Real-time CTF determination and correction. *J Struct Biol* **193**, 1–12 (2016).
38. Punjani, A., Rubinstein, J. L., Fleet, D. J. & Brubaker, M. A. cryoSPARC: algorithms for rapid unsupervised cryo-EM structure determination. *Nat Methods* **14**, 290–296 (2017).
39. Pettersen, E. F. et al. UCSF Chimera–a visualization system for exploratory research and analysis. *J Comput Chem* **25**, 1605–1612 (2004).
40. Emsley, P., Lohkamp, B., Scott, W. G. & Cowtan, K. Features and development of Coot. *Acta Crystallogr D Biol Crystallogr* **66**, 486–501 (2010).
41. Adams, P. D. et al. PHENIX: a comprehensive Python-based system for macromolecular structure solution. *Acta Crystallogr D Biol Crystallogr* **66**, 213–221 (2010).
42. Case, D. A. et al. The Amber biomolecular simulation programs. *J Comput Chem* **26**, 1668–1688 (2005).
43. Tian, C. et al. ff19SB: Amino-Acid-Specific Protein Backbone Parameters Trained against Quantum Mechanics Energy Surfaces in Solution. *J Chem Theory Comput* **16**, 528–552 (2020).
44. Wang, J., Wolf, R. M., Caldwell, J. W., Kollman, P. A. & Case, D. A. Development and testing of a general amber force field. *J Comput Chem* **25**, 1157–1174 (2004).
45. Wittayanarakul, K., Hannongbua, S. & Feig, M. Accurate prediction of protonation state as a prerequisite for reliable MM-PB(GB)SA binding free energy calculations of HIV-1 protease inhibitors. *J Comput Chem* **29**, 673–685 (2008).
46. Yu, R., Craik, D. J. & Kaas, Q. Blockade of neuronal alpha7-nAChR by alpha-conotoxin ImI explained by computational scanning and energy calculations. *PLoS Comput Biol* **7**, e1002011 (2011).

Acknowledgements

We thank X. Huang, B. Zhu, X. Li, L. Chen, and other staff members at the Center for Biological Imaging (CBI), Core Facilities for Protein Science at the Institute of Biophysics, Chinese Academy of Science (IBP, CAS) for the support in cryo-EM data collection; We thank Yan Wu for his research assistant service, and Zhao laboratory members for helpful discussions. This work was funded by Chinese National Programs for Brain Science and Brain-like Intelligence Technology (Grant No. 2022ZD0205800 to Y.Z.), the National Key Research and Development Program of China (Grant No. 2021YFA1301501 to Y.Z.), the Chinese Academy of Sciences Strategic Priority Research Program (Grant No. XDB37030304 to Y.Z.), the National Laboratory of Biomacromolecules, Institute of Biophysics, Chinese Academy of Sciences (Grant No. 2022kf09), and the National Natural Science Foundation of China (Grant No. 92157102 to Y.Z.). This work was supported by the grant from the National Natural Science Foundation of China (NSFC) (No. 82122064.), Qingdao Marine Science and Technology Center (No.2022QNLM030003-1), and Foundation of Shandong Province (No. 2022GJJLJRC02-046).

Author contributions

Y.Z. conceived and supervised the project. J.S., H.Z. and Y.M. carried out molecular cloning experiments, J.S. expressed and purified protein samples, and prepared samples for cryo-EM study. J.S. and R.L. and J.Z. carried out cryo-EM data collection. J.S. and Z.Y. processed the cryo-EM data. J.S. and Z.Y. built and refined the atomic model. J.S. and Z.Y. analyzed the structures and prepared the figures. Z.Y., R.Y., Z.Y. and J.S. designed the electrophysiological experiments. Z.Y. performed all two-electrode voltage clamp experiments. R.Y. and Z.Z conducted the molecular dynamics simulations. J.S. wrote the original draft of the manuscript. Z.Y., R.Y., J.S., Z.Y. and Y.G. edited the manuscript with input from all authors.

Competing interests

The authors declare no competing interests.

Additional information

Supplementary information The online version contains supplementary material available at https://doi.org/10.1038/s41467-025-58333-0.

Correspondence and requests for materials should be addressed to Rilei Yu or Yan Zhao.

Peer review information *Nature Communications* thanks the anonymous reviewers for their contribution to the peer review of this work. A peer review file is available.